

Bioresorbable Wireless Sensors as Temporary Implants for In Vivo Measurements of Pressure

Di Lu, Ying Yan, Yujun Deng, Quansan Yang, Jie Zhao, Min-Ho Seo, Wubin Bai, Matthew R. MacEwan, Yonggang Huang, Wilson Z. Ray, and John A. Rogers*

Pressures at targeted locations inside the human body serve as critically important diagnostic parameters for monitoring various types of serious or even potentially fatal medical conditions including intracranial, intra-abdominal, and pulmonary hypertension, as well as compartment syndromes. Implantable commercial sensors provide satisfactory accuracy and stability in measurements of pressure, yet surgical removal is required after recovery of the patient to avoid infections and other risks associated with long-term implantation. Sensors that dissolve in biofluids (or, equivalently, bioabsorb or bioresorb) avoid the need for such surgeries, yet current designs involve either hard-wired connections and/or fail to provide quantitative measurements over clinically relevant lifetimes. Here, a bioresorbable, wireless pressure sensor based on passive inductor-capacitor resonance circuits in layouts and with sets of materials that overcome these drawbacks is reported. Specifically, optimized designs offer sensitivity as high as ≈ 200 kHz mmHg⁻¹ and resolution as low as 1 mmHg. Encapsulation approaches that use membranes of Si₃N₄ and edge seals of natural wax support stable operation in vivo for up to 4 days. The bioresorbable pressure sensing technology reported here may serve as an important solution to temporary, real-time monitoring of internal pressure for various medical conditions.

1. Introduction

Measurements of pressures in closed compartments and lumina of the body, such as in the intracranial space, the abdominal cavity, the arteries and the osteofascial compartments, can provide essential diagnostic information in the context of many life-threatening medical conditions. For example, a rise of intracranial pressure (ICP) by 5–10 mmHg after a traumatic brain injury may impede blood flow and lead to ischemias that demand immediate medical intervention.^[1] Intra-abdominal hypertension, corresponding to pressures higher than 12 mmHg, leads to increased morbidity for critically ill patients.^[2] Pulmonary hypertension, as defined by >25 mmHg pressure in the pulmonary artery, is associated with many serious heart and lung conditions.^[3] An intra-compartmental pressure of 30 mmHg or more indicates compartment syndromes that may lead to devastating sequelae.^[4] Although certain pressures with clinical significance, such as blood pressure, are externally accessible, measurements of most

internal pressures involve implantable sensing devices, with commercial examples for ICP^[5] and pulmonary artery pressure.^[6] These platforms require surgical removal after recovery of the patient, to avoid infections and other health risks related to long-term implantation.^[7] Various complications as well as distress associated with these procedures motivate alternative approaches based on implantable pressure sensors constructed with bioresorbable materials.^[8–10] A range of metals,^[11] semiconductors and their derivatives,^[12,13] polymers,^[14] and biomolecules,^[15] form the foundations for such technologies, where appropriate designs allow dissolution and resorption of the device entirely, without a trace, after a controlled period, thus naturally eliminating the necessity for extraction surgeries.^[8–10]

Several such bioresorbable pressure sensors rely on percutaneous wires for data acquisition, which introduce risks of infections and restrict natural movements of the patient.^[8,16] Wireless sensors, typically based on inductor–capacitor (LC) circuits, circumvent these disadvantages.^[17,18] Here, a change of a parameter of interest induces a change of the capacitance, and thus the resonance frequency of the circuit, which can be detected by wireless coupling to an external antenna.

Dr. D. Lu, Q. Yang, Dr. J. Zhao, Dr. M.-H. Seo, Dr. W. Bai, Prof. J. A. Rogers

Querrey Simpson Institute for Bioelectronics
Northwestern University
Evanston, IL 60208, USA
E-mail: jrogers@northwestern.edu

Dr. Y. Yan, Prof. M. R. MacEwan, Prof. W. Z. Ray
Department of Neurological Surgery
Washington University School of Medicine
St Louis, MO 63110, USA

Dr. Y. Deng
State Key Laboratory of Mechanical System and Vibration
Shanghai Jiao Tong University
Shanghai 200240, China

Dr. Y. Deng, Prof. Y. Huang
Departments of Mechanical Engineering
Civil and Environmental Engineering
and Materials Science and Engineering
Northwestern University
Evanston, IL 60208, USA

 The ORCID identification number(s) for the author(s) of this article can be found under <https://doi.org/10.1002/adfm.202003754>.

DOI: 10.1002/adfm.202003754

This approach requires no active components, and the passive operation eliminates the need for batteries or energy harvesting systems.^[8,19] A recent publication described systems of this general type, but without demonstrations of quantitative measurements in vivo^[17] and with operational stability of only a few minutes,^[17] likely limited by fast degradation of key materials and/or water permeation through them. Realistic medical applications demand stable, quantitative, and real-time pressure sensing on meaningful timescales (days).^[1]

This work introduces the design aspects, fabrication procedures, performance characteristics, in vivo operational capabilities, and degradation processes associated with a bioresorbable, passive, wireless pressure sensing device based on the LC resonance of a coil inductor and an air-cavity-type parallel plate capacitor sensor. Properly designed air cavities and minimized parasitic capacitances allow sensitivities ≈ 200 kHz mmHg⁻¹, and resolution of 1 mmHg. Bioresorbable water barrier structures that combine Si₃N₄ nanomembranes with natural wax edge seals prevent water permeation, to ensure stable operation. Studies in rat models indicate that the resulting platforms can provide quantitative, high-resolution pressure measurements of ICP over several days, with performance that is comparable to non-resorbable, wired, commercial sensors currently used for clinical applications.

2. Results and Discussion

Figure 1 illustrates the principle of the LC-circuit-based wireless pressure sensor. A deformable, conductive membrane converts

the pressure of surrounding fluids to a mechanical response. Pairing this membrane with a fixed electrode forms a parallel plate capacitor that, in turn, converts this bending deformation into a change in capacitance according to (Figure 1a):

$$C(p) = C_s + C_p = \epsilon_0 \epsilon_r \frac{A}{b(p)} + C_p \quad (1)$$

where ϵ_0 is the vacuum permittivity, $\epsilon_r \approx 1$ is the dielectric constant of the medium (air) between the plates, A is the area of the plates, b is the average separation between the plates, p is the applied pressure, and C_s , C_p are the sensor and parasitic capacitance in the circuit, respectively. Connecting the capacitor to an inductor (inductance L with resistance R , Figure 1b) converts changes in capacitance to changes in resonance frequency ($f_s(p) = 1/2\pi\sqrt{LC(p)}$). Coupling of L to an alternating magnetic field induced by passing radiofrequency power through a readout coil L_0 (Figure 1b,c) and measuring the real part of the impedance ($\text{Re } Z$) across L_0 as a function of frequency yields a peak at a frequency f_s . Fitting the peak using the following equation deduced from the equivalent circuit (Figure 1b) yields the value of f_s ^[20]:

$$\text{Re } Z = \frac{kf^2}{1 + Q^2(f/f_s - f_s/f)^2} \quad (2)$$

where $Q = \frac{1}{R}\sqrt{\frac{L}{C}}$ is the quality factor and k is the coupling constant depending on the relative position between L and L_0 . Measuring f_s at different pressures gives a calibration function

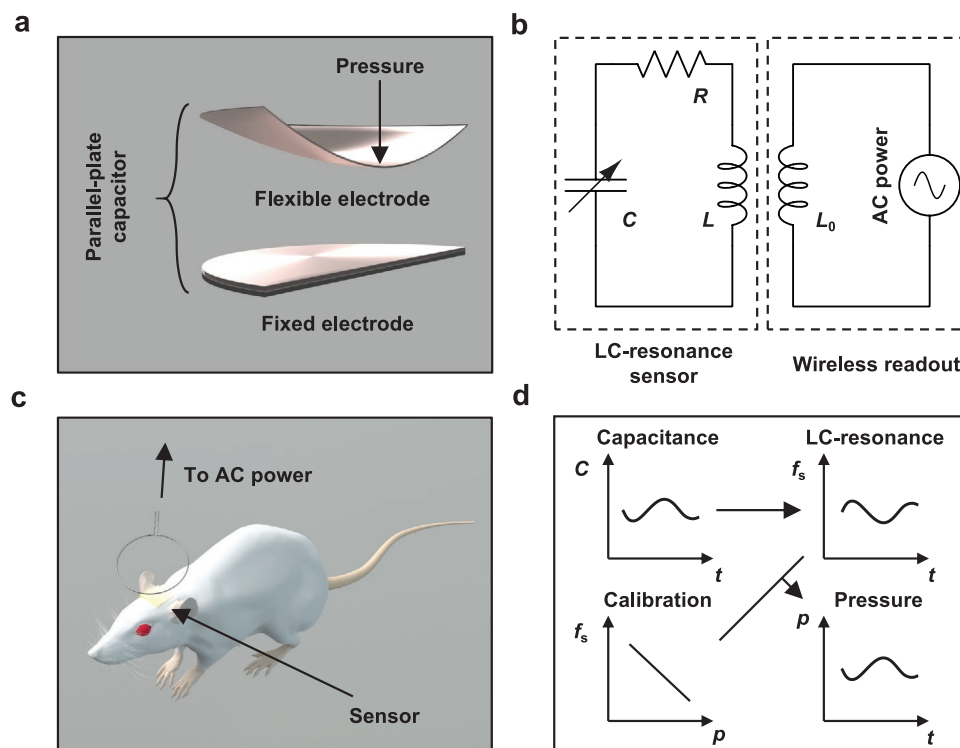


Figure 1. Schematic illustrations, circuit diagrams, principles of operation, and animal model application of bioresorbable, passive, wireless sensors of pressure. a) Illustration of the structure of a parallel-plate capacitor with flexible and fixed electrodes to yield a pressure-dependent capacitance C . b) Equivalent circuit of the LC-resonance sensor and the wireless readout system. c) Schematic illustration of wireless sensing of intracranial pressure based on an implanted LC-resonance sensor coupled to an external readout coil. d) Flowchart for the signal conversion process.

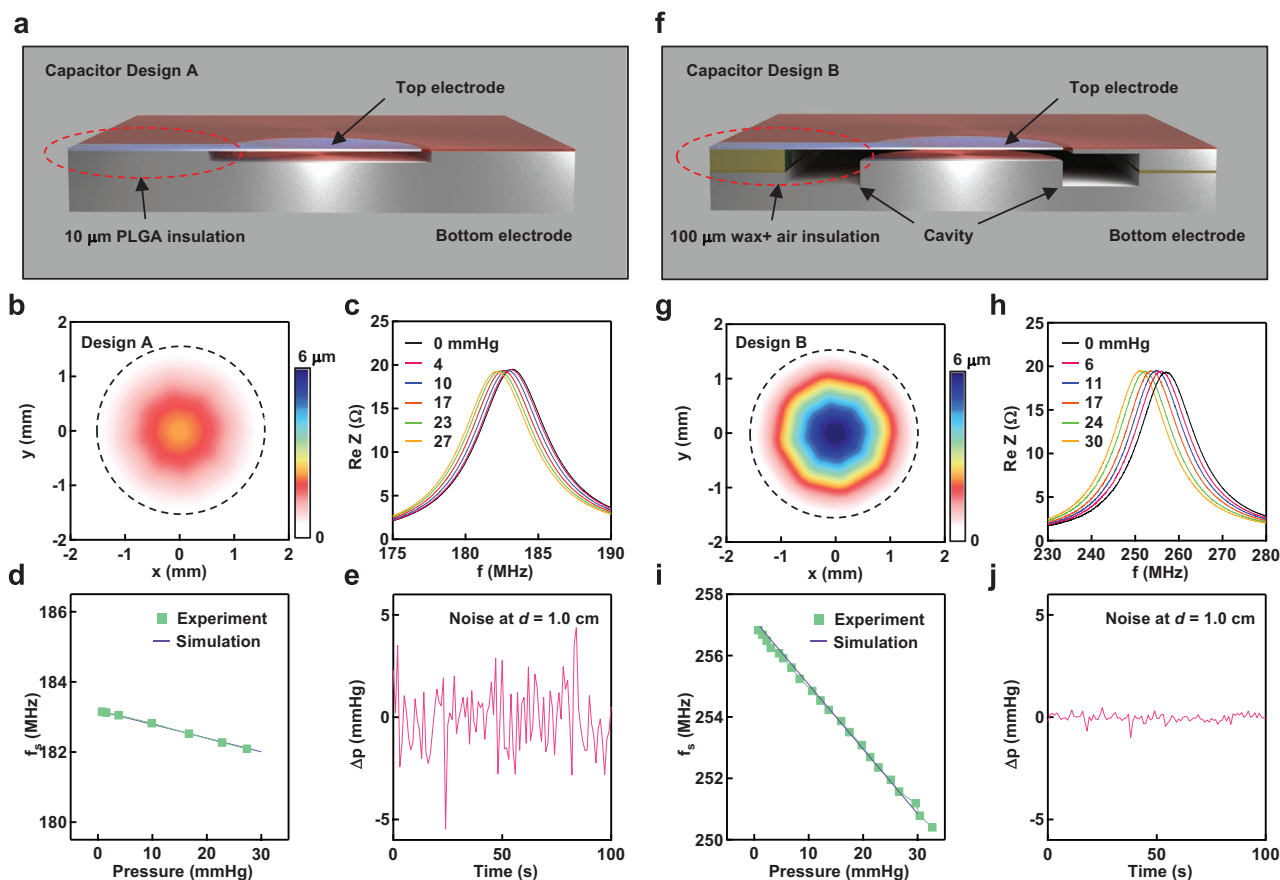


Figure 2. Designs for pressure-sensitive capacitors and results from their use in passive wireless sensors. a) Schematic illustration of Design A. b) Contour map of the simulated vertical displacements of the top electrode in Design A at 10 mmHg. The dashed circle indicates the boundary of the top electrode. c) Wireless measurements of the real part of the impedance (Z) as a function of frequency (f), to define the LC -resonance peak (f_s) for Design A. d) Simulation and measurement results for the dependence of f_s on pressure (p), to define the calibration curve $f_s(p)$ for Design A. e) Measurements of the change in p (Δp) as a function of time during static conditions, to define the magnitude of the noise associated with Design A. f–j) Results for Design B, analogous to those for Design A in (c–e).

$f_s(p)$. Converting a time series of measured f_s to pressure using this function serves as the basis for real-time monitoring of pressure (Figure 1d). Such LC -resonance mechanisms are not suitable for cases that involve relative movement between L and L_0 , as accurate fitting of f_s requires a stable coupling constant k during the frequency scan. Nevertheless, this approach is sufficient for critical medical conditions, as highlighted in the introduction, given that patients in these scenarios must remain in hospital beds, without significant freedom of movement. Achieving sensors for ambulatory patients or in other contexts may require alternative designs such as those that exploit digital wireless communication protocols.

As described above, the most direct approach to realize the pressure sensitive capacitor is to integrate a flexible electrode on a fixed electrode constructed as a trench on the surface of a substrate (Design A, Figure 2a). Here the flexible electrode is a Zn foil (2 μm) embedded at the neutral mechanical plane of a membrane of poly(lactic-co-glycolic acid) (PLGA, 10 μm thick), while the fixed electrode consists of a trench etched into the surface of a foil of Mg (50 μm depth, Experimental Section). Theoretical modeling of the flexible membrane (Experimental Section), accounting for the air pressure increase in the cavity

according to the ideal gas law, quantifies its deformation under applied pressure (Figure 2b). Connecting the capacitor to a Mg spiral coil inductor yields a resonator circuit, with a resonance frequency f_s that depends on pressure (Figure 2c). Demonstrations of measurements of ICP with rat models dictate the choice of the size of the coil (outer diameter 8 mm, Figure S1, Supporting Information). The calibration function $f_s(p)$ is linear and the sensitivity of the sensor (df_s/dp) is 40 kHz mmHg⁻¹, consistent with the theoretical model (Figure 2d). Scanning the frequency around the resonance peak every 1 s, fitting the peak to yield f_s , and converting $f_s(t)$ to $p(t)$ using the calibration function support real-time monitoring of the pressure. Measuring atmospheric pressure at a fixed wireless transmission distance (1 cm, a typical implantation depth in biomedical applications) establishes the baseline of electrical noise (Figure 2e). The results indicate that magnitude of the noise corresponds to pressures (5 mmHg) that are comparable to those that are clinically significant.^[1–3] As such, the resolution provided by this design may not be sufficient for practical use.

Increasing the measurement time can reduce the noise (such as 1 min, Figure S2, Supporting Information), but at the expense of time resolution. An alternative approach involves

increasing the sensitivity df_s/dp without increasing the noise in f_s (Δf_s), to suppress the noise in p . Specifically, given that $f_s(p)$ is linear, the ratio between the noise in the resonance frequency and the noise in the pressure $\Delta f_s/\Delta p$ should be equal to the df_s/dp . The sensitivity satisfies the following equation:

$$\frac{df_s}{dp} = -\frac{f_s}{2C} \frac{dC}{dp} = -\frac{f_s}{2(C_s + C_p)} \frac{dC_s}{dp} = \frac{C_s}{2(C_s + C_p)} \frac{f_s}{b} \frac{db}{dp} \quad (3)$$

This expression indicates that reducing the parasitic capacitance C_p and increasing the absolute value of the deformation of the flexible electrode per unit pressure db/dp will increase the sensitivity. One of the main sources of C_p is the overlap between the top and bottom electrodes at the edge of the capacitor (Figure 2a). This contribution can be reduced by removing part of the bottom electrode to increase the distance between the two electrodes (Figure 2f). Strategies for increasing the absolute value of db/dp can be identified by modeling the average separation of the plates as a function of the applied pressure (Experimental Section, Figure S3, Supporting Information):

$$b = h - \frac{p}{\frac{192D}{R^4} + \frac{p_0}{V_0/\pi R^2}} \quad (4)$$

where $h = 50 \mu\text{m}$ is the initial separation between the plates before the pressure p is applied, $D = 0.00033 \text{ N mm}$ and $R = 1.5 \text{ mm}$ are the bending stiffness and the radius of the membrane, p_0 and V_0 are the pressure (1 atm) and the volume of the cavity, respectively. The terms $\frac{192D}{R^4}$ and $\frac{p_0}{V_0/\pi R^2}$ in the above equation represent the resistance to deformation due to the bending stiffness of the membrane and the pressure increase in the cavity according to the ideal gas law, respectively. For Design A, $V_0 = 0.35 \text{ mm}^3$ such that $\frac{p_0}{V_0/\pi R^2} = 2.02 \text{ N mm}^{-3}$ dominates (much larger than $\frac{192D}{R^4} = 0.0125 \text{ N mm}^{-3}$), i.e., the resistance to deformation mainly comes from the pressure increase in the cavity. As a result, increasing V_0 (to 1.15 mm^3 for Design B, Figure 2f and Figure S1, Supporting Information) to decrease $\frac{p_0}{V_0/\pi R^2}$ without changing other parameters (e.g., materials properties, thicknesses of the top electrode, plate area A , and initial separation h (Figure 2f)) effectively increases the deformation of the top electrode, therefore the sensitivity of the device, for a given applied pressure (Figure 2g; Figures S3 and S4, Supporting Information).

Design B (Figure 2f) incorporates these schemes for reducing C_p and increasing the absolute value of db/dp . The sensitivity of Design B is 5 times higher than that of the Design A ($207 \text{ kHz mmHg}^{-1}$). With similar Δf_s (Figure S5, Supporting Information), this design reduces the baseline noise by a similar factor, to a value of 1 mmHg (Figure 2h–j), thereby satisfying requirements for monitoring pressures in ranges relevant for applications in clinical care. Figure S1, Supporting Information, also shows the detailed dimensions of the capacitor designs. The maximum pressure that can be measured by this sensor is (See Experimental Section)

$$p_{\max} = \frac{h}{3} \left(\frac{192D}{R^4} + \frac{p_0}{V_0/\pi R^2} \right) \quad (5)$$

For the initial separation $h = 50 \mu\text{m}$, it gives 256 mmHg for Design A and 79 mmHg for Design B.

The construction of these devices involves the assembly of coil inductors and capacitive sensors of Design B with encapsulation layers as water barriers (Figure 3a,b). Laser cutting foils of Mg yields spiral coil inductors ($100 \mu\text{m}$ thick; Figure 3a) and components (bottom electrode, $250 \mu\text{m}$; spacer, $100 \mu\text{m}$) of the capacitor (Figure 3a, center; Experimental Section). Sandwiching a laser cut Zn foil ($2 \mu\text{m}$) between two layers of PLGA ($5 \mu\text{m}$ each) followed by hot pressing produces the top flexible electrode (Figure 3a, center). Assembling the capacitive sensor involves attaching the bottom electrode and the spacer with bioresorbable wax and adhering to the top electrode by treating the bottom surface of the bottom layer of PLGA with ethyl acetate vapor to improve the bonding to the spacer (Figure 3a, center, Experimental Section). Electrically connecting the coil to the sensor using conductive wax (mixture of W powder and wax, Experimental Section) yields an LC-resonance circuit (Figure 3a). Laminating a freestanding membrane of Si_3N_4 ($2 \mu\text{m}$) on the top electrode and applying a coating of bioresorbable wax ($\approx 500 \mu\text{m}$) around the perimeter of the sensor, but not on the top electrode, completes the fabrication (Figure 3a,c). Si_3N_4 membranes thinner than $\approx 2 \mu\text{m}$ are fragile and easily fracture in the membrane transfer process, while thicker Si_3N_4 membranes may significantly alter the mechanical properties of the top flexible electrodes.^[10] The Si_3N_4 and wax serve as bioresorbable biofluid barriers that enable stable operation for a few days in vivo.^[10,12,15] Systematic tests (Experimental Section) indicate that the performance of the resulting sensor is comparable to that of a clinical standard device for monitoring ICP (Figure 3d). Figure S6, Supporting Information, illustrates the noise level of design B as a function of relative position between the readout coil and the sensor.

Implanting the sensor in a rat model demonstrates quantitative, real-time measurement of the ICP for 4 days. Attaching the sensor over a burr hole drilled through the skull connects the cranial cavity to the pressure sensing membrane, thereby allowing for measurements of ICP (Figure 4a,b). Some drift of the baseline occurs during the first day after implantation (Figure S7a, Supporting Information) likely due to transient processes of bleeding, flowing of interstitial and cerebrospinal fluids, coagulation, and drying, with associated changes in the dielectric environment around the capacitor (dielectric constant of water ≈ 80 ; Figure S7b, Supporting Information). Stable recordings are possible after this initial timeperiod. Squeezing the flank of the rat induces detectable changes in ICP across an expected range (Figure 4c). This process mimics increases in ICP due to intra-abdominal hypertension: compressing the abdominal cavity increases the intra-abdominal pressure, which in turn increases the ICP.^[21] Indeed, the changes in pressure inferred from changes in f_s agree well with those measured simultaneously using a commercial wired ICP sensor that is also inserted into the cranial cavity (Figure 4d). The baseline noise corresponds to $\approx 1 \text{ mmHg}$, similar to the results observed in vitro. The sensor exhibits stable operation from the second day to the fifth day (1–4 d, Figure 4d), with some drift in the baseline after 4 d, likely due to some slight amount of water permeation through the encapsulation layers. The result suggests that the change in resonance frequency 1–4 d after implantation is due to real

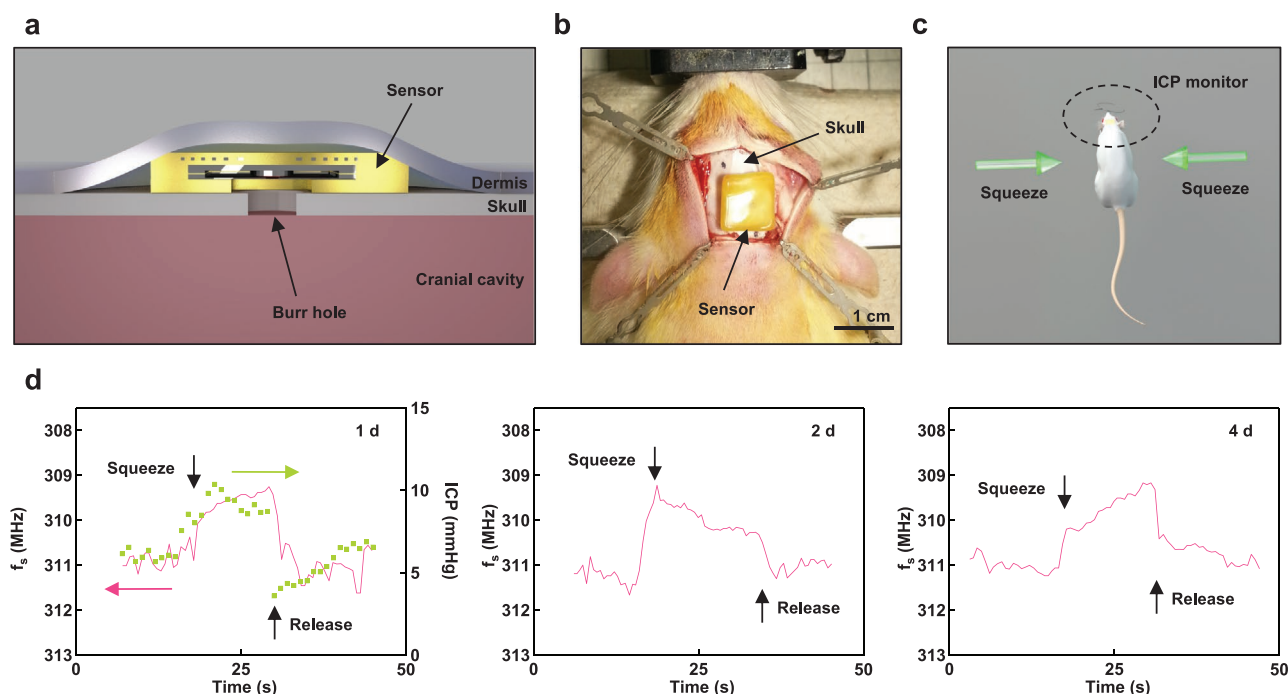


Figure 4. Wireless measurements of intracranial pressure (ICP) on a rat model. a) Schematic illustration of the cross section of the sensor showing its placement over a burr hole through the skull to allow coupling to the fluids in the intracranial space. b) Image of the implanted sensor prior to suturing the surgical site. c) Schematic illustration of the procedure for squeezing the flanks of the animal. d) Measurements of ICP obtained using the bioresorbable wireless sensor at 1 d, 2 d, and 4 d after implantation, and corresponding measurements using a commercial wired sensor at 1 d. To minimize health risks such as mechanical damage and infections, the wired commercial ICP sensor was extracted after 1 d.

physiological ICP signals. Previous studies also report similar drifts and stabilization behaviors in non-resorbable capacitive pressure sensors.^[22]

As mentioned previously, a key feature of this platform is that all of the constituent materials are bioresorbable. **Figure 5** highlights the relevant chemical and physical processes in phosphate

buffered saline at 37 °C. The Mg and Zn react with water to form soluble hydroxides ($\text{Mg} + 2\text{H}_2\text{O} \rightarrow \text{Mg}(\text{OH})_2 + \text{H}_2$, $\text{Zn} + 2\text{H}_2\text{O} \rightarrow \text{Zn}(\text{OH})_2 + \text{H}_2$).^[11] The W in the conductive wax oxidizes in water to yield a soluble acid ($2\text{W} + 2\text{H}_2\text{O} + 3\text{O}_2 \rightarrow 2\text{H}_2\text{WO}_4$).^[11] The Si_3N_4 reacts with water to give silicic acid and ammonia ($\text{Si}_3\text{N}_4 + 12\text{H}_2\text{O} \rightarrow 3\text{Si}(\text{OH})_4 + 4\text{NH}_3$).^[12] The PLGA hydrolyzes

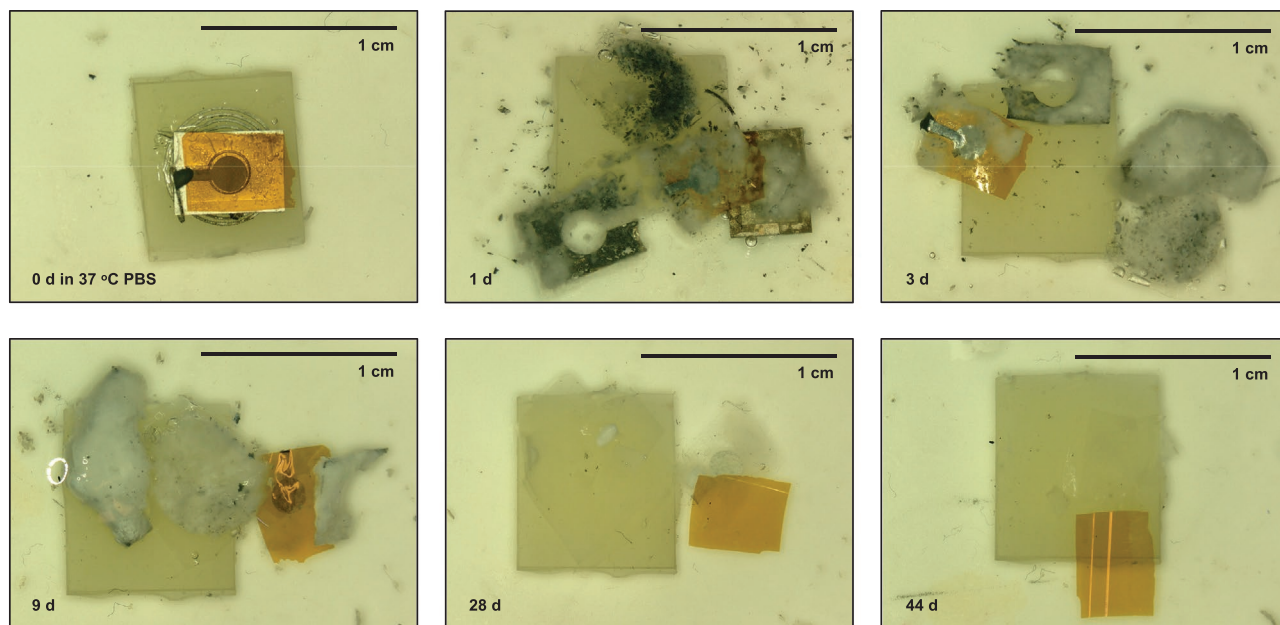


Figure 5. Degradation of a pressure sensor in 37 °C PBS (solution refreshed every 2 days).

into lactic and glycolic acid and dissolves,^[14] while the biocompatible wax degrades slowly in vivo.^[15] Removing the front side of the wax encapsulation layer allows for direct observation of the internal structure. The sensor disintegrates, gradually dissolves, and leaves only the Si₃N₄ membrane and the wax encapsulation after 44 d (Figure 5). The rate of degradation of the Si₃N₄ and wax are 4.5–30 nm per month and 10 μm per month, respectively,^[12,15] such that complete degradation of these components of the device will occur over several to many months. Previous reports verify the biocompatibility of the constituent bioresorbable materials,^[23,24] and show that the in vivo degradation behaviors of the constituent materials are similar to the in vitro cases.^[15,24]

3. Conclusion

The material approaches and sensor designs reported here serve as the basis of an attractive technology solution for temporary measurements of liquid pressures at targeted locations in the body. Being constructed entirely from bioresorbable materials, these sensors operate stably for a relevant period of time but ultimately dissolve completely in biofluids, thus avoiding the extraction surgeries that are necessary for their non-resorbable, commercial counterparts. The passive LC-resonance mechanism for sensing enables battery-free operation, with a simple sensor structure. Improving the design of the pressure-dependent capacitor, namely increasing the volume of the air cavity and reducing the parasitic capacitance, allows for levels of accuracy and precision necessary for clinical applications. Encapsulation schemes that exploit Si₃N₄ membranes and natural wax allow for stable operation for 4 days in a rat model, with performance similar to that of a commercial wired sensor. The approaches reported here suggest additional applications, including those in temporary monitoring of intra-abdominal, intracompartmental, and pulmonary pressures.

4. Experimental Section

Fabrication of the Pressure Sensors: Laser cutting foils of Mg with thicknesses of 100 μm yielded spiral coils, Mg wires, and Mg spacers. Laser cutting similar foils with thicknesses of 250 μm yielded Mg bottom electrodes. Etching these components using 20 v% acetic acid for 5 s removed the surface oxide layers. Adhesion between the Mg spacers and bottom electrodes (Figure 3a,b) relied on candelilla wax (Sigma-Aldrich), temporarily melted at 80 °C. Sandwiching laser-cut foils of Zn (2 μm, electron beam evaporation on a temporary substrate) between two sheets of PLGA (5 μm, 65:35, M_w = 40 000–75 000, Sigma-Aldrich) followed by hot-pressing at 80 °C for 10 min formed the top electrodes. Adhering the front side of the top electrode onto a sheet of polydimethylsiloxane (PDMS) and treating the backside in a vapor of ethyl acetate at 60 °C for 5 s softened the PLGA and improved the adhesion to the Mg spacer. Immediately laminating the top electrode on the Mg spacer, evaporating the residual ethyl acetate for ≈1 h, and removing the PDMS formed the capacitor (Figure 3a,b). Electrically conductive wax, consisting of a mixture of tungsten powder (C10, buffalo tungsten) and candelilla wax in a weight ratio 15:1, applied at the joints of the inductors and the capacitors completed the LC circuits (Figure 3a,b).^[15] A sheet of PLGA inserted between the Mg coil and the bottom electrode insulated the circuits (Figure 3a,b). Figure S1, Supporting Information, summarizes the detailed dimensions of the above components. The devices exploit different metals to satisfy different requirements. The ease of depositing

thin films with low resistance, and low bending stiffness makes Zn an excellent candidate for the flexible top electrodes; the fast degradation rates of Mg make this metal ideal for thick conductors needed for coils with higher Q-factor, and for bottom electrodes and spacers; the ability to form conductive wax makes powders of W suitable for electrical interconnects.

Encapsulation of the Sensors: Spin coating photoresist (AZ4620, 1000 rpm for 1 min) on a Si₃N₄ film (2 μm, by low-pressure chemical vapor deposition) formed on a silicon wafer (500 μm) yielded a protective layer. Deep reactive ion etching (STS LpX Pegasus) the backside of the wafer etched part of the Si crystal (200–300 μm) and expedited the subsequent chemical etching process. Cutting the wafers to pieces with dimensions to match those of the capacitors (5 × 7 mm²) and immersing them in 30 wt% KOH solution at 85 °C for 8–16 h eliminated the wafers and dissolved the photoresist to yield free floating membranes of Si₃N₄. Rinsing the membranes in water and transferring them onto the surfaces of the capacitors formed protective barriers for water penetration. Adhering a piece of PDMS (1 mm thickness) with lateral dimensions slightly smaller than those of the capacitor protected the pressure sensing membrane from the wax used in subsequent steps. Here, dip-coating the sensor in a molten mixture of beeswax (refined, Sigma-Aldrich) and candelilla wax at a weight ratio 2:3 at 85 °C for 5 cycles yielded a ≈500-μm-thick encapsulation layer.^[10] Blowing the fabricated sensor with hot air using a heat gun softened the wax and eliminated local defects in the coating. Removing the protective piece of PDMS exposed the sensing membrane, to complete the fabrication.

Signal Readout and Pressure Measurements: The readout system consisted of a single turn coil (Figure S1, Supporting Information) connected to an Agilent E5062A or an Agilent portable N9923A vector network analyser (VNA). Setting the VNA to reflective mode allowed measurement of the real and imaginary parts of the S-matrix element S₁₁. The real part of the impedance across L₀ was then deduced from the following formula:

$$\text{Re}Z = Z_0 \frac{1 - (\text{Re}S_{11})^2 - (\text{Im}S_{11})^2}{(1 - \text{Re}S_{11})^2 + (\text{Im}S_{11})^2} \quad (6)$$

where Z₀ is 50 Ω. Placing the sensors in the barrel of a syringe (BD, 30 mL) connected to a commercial pressure sensor (Neulog) allowed the measurement of resonance frequency under different pressures.

Deformation of the Top Electrode: A theoretical model, accounting for the air pressure increase in the cavity according to the ideal gas law, is established for the deformation of the top electrode due to the pressure on the device. Let \bar{w} denote the average displacement of the membrane. The volume of the cavity below the top electrode is reduced by $\pi R^2 \bar{w}$ (R: radius of the top electrode). The ideal gas law for a constant temperature, $p_0 V_0 = (p_0 + \Delta p)(V_0 - \pi R^2 \bar{w})$, gives the air pressure increase Δp in the cavity as

$$\Delta p = p_0 \frac{\bar{w}}{(V_0 / \pi R^2) - \bar{w}} \quad (7)$$

where p₀ is the atmosphere pressure and V₀ is the initial volume of the cavity.

The membrane is modeled as a circular plate subjected to pressure p and Δp on the top and bottom surfaces, respectively. In terms of the vertical displacement w, the plate theory in the polar coordinate r requires

$$D \left(\frac{d^2}{dr^2} + \frac{1}{r} \frac{d}{dr} \right) \left(\frac{d^2}{dr^2} + \frac{1}{r} \frac{d}{dr} \right) w = p - \Delta p \quad (8)$$

where D is the bending stiffness given by

$$D = \frac{E_{Zn} t_{Zn}^3}{12(1 - \nu_{Zn}^2)} + \frac{E_{PLGA}}{12(1 - \nu_{PLGA}^2)} \left[(2t_{PLGA} + t_{Zn})^3 - t_{Zn}^3 \right] \quad (9)$$

for a 3-layer symmetric composite plate (PLGA-Zn-PLGA with the thickness of $5\ \mu\text{m}$ – $2\ \mu\text{m}$ – $5\ \mu\text{m}$), where t is the thickness, E and ν are the modulus and Poisson's ratio, respectively, with the relevant subscript for PLGA layer ($E_{\text{PLGA}} = 1.6\ \text{GPa}$, $\nu_{\text{PLGA}} = 0.34$ and $t_{\text{PLGA}} = 5\ \mu\text{m}$) and Zn layer ($E_{\text{Zn}} = 100\ \text{GPa}$, $\nu_{\text{Zn}} = 0.25$ and $t_{\text{Zn}} = 2\ \mu\text{m}$). The boundary conditions are $w = 0$ and $dw/dr = 0$ at the radius $r = R$. The solution of the above equation is

$$w = \frac{p - \Delta p}{16D} \left[\frac{1}{4}(r^4 - R^4) - \frac{1}{2}R^2(r^2 - R^2) \right] \quad (10)$$

The average \bar{w} is obtained as

$$\bar{w} = \frac{2}{R^2} \int_0^R wr dr = \frac{R^4}{192D} (p - \Delta p) \quad (11)$$

Substitution of Δp from the ideal gas law into the above equation gives a nonlinear relationship between the average displacement \bar{w} of the top electrode and the applied pressure p as

$$\bar{w} = \frac{2p}{\frac{192D}{R^4} + \frac{p + p_0}{V_0/\pi R^2} + \sqrt{\left(\frac{192D}{R^4} + \frac{p + p_0}{V_0/\pi R^2}\right)^2 - 4\frac{192D}{R^4} \frac{p}{V_0/\pi R^2}}} \quad (12)$$

For small applied pressure such that $\bar{w} \ll V_0/\pi R^2$, the above nonlinear relation degenerates to a linear relation as

$$\bar{w} = \frac{p}{\frac{192D}{R^4} + \frac{p_0}{V_0/\pi R^2}} \quad (13)$$

and the differences of \bar{w} obtained from the exact solution and linear approximation are less than 4% at $p < 30\ \text{mmHg}$, for Design A and B (Figure S3, Supporting Information). For the initial separation $h = 50\ \mu\text{m}$ in the experiments, the average separation of the plates b under the applied pressure p is then given by Equation (4). The displacement of the top electrode is then obtained as

$$w = \frac{p}{\frac{192D}{R^4} + \frac{p_0}{V_0/\pi R^2}} \frac{1}{R^4} \left[3(r^4 - R^4) - 6R^2(r^2 - R^2) \right] \quad (14)$$

and its maximum (at the center $r = 0$) is $w_{\text{max}} = 3\bar{w}$. The above analysis only holds $w_{\text{max}} < h$, which leads to the maximum pressure in Equation (5) that can be measured by this pressure sensor.

Studies on Animal Models: All procedures associated with the animal studies followed the recommendations in the Guide for the Care and Use of Laboratory Animals of the National Institutes of Health. The Institutional Animal Care and Use Committee (IACUC) of Washington University in St Louis approved the protocol (protocol no. 20 170 189). A male Lewis rat weighing 250–350 g (Charles River) received subcutaneous injections of buprenorphine hydrochloride ($1.2\ \text{mg kg}^{-1}$; Reckitt Benckiser Healthcare) for pain management 1 h before the surgical process. The surgical procedures involved anaesthetizing the rat with isoflurane gas inhalation (4% for induction and 2% for maintenance), holding the head in a stereotaxic frame. The implantation process of the sensor included subsequent preparation and sterilization of the head region, creation of a craniectomy on the head region, and implantation of the bioresorbable sensor on the skull. Applying dental cement (Fusio Liquid Dentin) and curing under ultraviolet light secured the implant on the skull and made the sensor airtight. A commercial ICP sensor (Camino) implanted in nearby craniectomy enabled the evaluation of the accuracy of ICP measured by the wireless sensor. Squeezing the flank of the rat under anesthesia by hand to increase the ICP by 5–10 mmHg for 15 s then releasing this compression induces a change in the ICP. The body temperature of the rat when conducting

the ICP measurements, monitored by a rectal probe, was $35.5\ ^\circ\text{C}$. The wireless readout involves a readout coil placed on top of the head, with a fixed working distance of $\approx 1\ \text{cm}$. The measurements are performed under anesthesia.

Supporting Information

Supporting Information is available from the Wiley Online Library or from the author.

Acknowledgements

This work utilized Northwestern University Micro/Nano Fabrication Facility (NUFAB) of Northwestern University's NUANCE Center, which has received support from Soft and Hybrid Nanotechnology Experimental (SHyNE) Resource (NSF ECCS-1542205), the Materials Research Science and Engineering Center (NSF DMR-1720139) at the Materials Research Center, the International Institute for Nanotechnology (IIN), the Keck Foundation, the State of Illinois through the IIN, and Northwestern University, and the Querrey-Simpson Institute for Bioelectronics.

Conflict of Interest

The authors declare no conflict of interest.

Keywords

biomedical implants, bioresorbable devices, in vivo pressure, transient electronics, wireless sensors

Received: April 29, 2020

Revised: June 14, 2020

Published online: August 9, 2020

- [1] M. Czosnyka, J. D. Pickard, *J. Neurol. Neurosurg. Psych.* **2004**, *75*, 813.
- [2] a) M. L. Cheatham, M. Malbrain, A. Kirkpatrick, M. Sugrue, M. Parr, J. De Waele, Z. Balogh, A. Leppaniemi, C. Olvera, R. Ivatury, S. D'Amours, J. Wendon, K. Hillman, A. Wilmer, *Inten. Care Med. Exp.* **2007**, *33*, 951; b) M. Malbrain, M. L. Cheatham, A. Kirkpatrick, M. Sugrue, M. Parr, J. De Waele, Z. Balogh, A. Leppaniemi, C. Olvera, R. Ivatury, S. D'Amours, J. Wendon, K. Hillman, K. Johansson, K. Kolkman, A. Wilmer, *Inten. Care Med.* **2006**, *32*, 1722.
- [3] N. Galie, M. M. Hoepfer, M. Humbert, A. Torbicki, J. L. Vachiery, J. A. Barbera, M. Beghetti, P. Corris, S. Gaine, J. S. Gibbs, M. A. Gomez-Sanchez, G. Jondeau, W. Klepetko, C. Opitz, A. Peacock, L. Rubin, M. Zellweger, G. Simonneau, *Eur. Heart J.* **2009**, *30*, 2493.
- [4] S. J. Mubarak, A. R. Hargens, W. H. Akeson, C. A. Owen, L. P. Garetto, *J. Bone Joint Surg.* **1978**, *60*, 1091.
- [5] M. Harary, R. G. F. Dolmans, W. B. Gormley, *Sensors* **2018**, *18*, 465.
- [6] J. T. Heywood, R. Jermy, D. Shavelle, W. T. Abraham, A. Bhimaraj, K. Bhatt, F. Sheikh, E. Eichorn, S. Lamba, R. Bharmi, R. Agarwal, C. Kumar, L. W. Stevenson, *Circulation* **2017**, *135*, 1509.
- [7] a) J. A. Rebeck, K. R. Murry, D. H. Rhoney, D. B. Michael, W. M. Coplin, *J. Neurol. Neurosurg. Psych.* **2000**, *69*, 381; b) A. Reghunathan, J. F. B. Chick, J. J. Gemmete, A. Hage, J. Mahn, M. S. Khaja, R. N. Srinivasa, *Radiol. Case Rep.* **2018**, *13*, 386.

- [8] S. K. Kang, R. K. Murphy, S. W. Hwang, S. M. Lee, D. V. Harburg, N. A. Krueger, J. Shin, P. Gamble, H. Cheng, S. Yu, Z. Liu, J. G. McCall, M. Stephen, H. Ying, J. Kim, G. Park, R. C. Webb, C. H. Lee, S. Chung, D. S. Wie, A. D. Gujar, B. Vemulapalli, A. H. Kim, K. M. Lee, J. Cheng, Y. Huang, S. H. Lee, P. V. Braun, W. Z. Ray, J. A. Rogers, *Nature* **2016**, 530, 71.
- [9] a) K. J. Yu, D. Kuzum, S. W. Hwang, B. H. Kim, H. Juul, N. H. Kim, S. M. Won, K. Chiang, M. Trumpis, A. G. Richardson, H. Cheng, H. Fang, M. Thomson, H. Bink, D. Talos, K. J. Seo, H. N. Lee, S. K. Kang, J. H. Kim, J. Y. Lee, Y. Huang, F. E. Jensen, M. A. Dichter, T. H. Lucas, J. Viventi, B. Litt, J. A. Rogers, *Nat. Mater.* **2016**, 15, 782; b) J. Shin, Y. Yan, W. Bai, Y. Xue, P. Gamble, L. Tian, I. Kandela, C. R. Haney, W. Spees, Y. Lee, M. Choi, J. Ko, H. Ryu, J. K. Chang, M. Pezhouh, S. K. Kang, S. M. Won, K. J. Yu, J. Zhao, Y. K. Lee, M. R. MacEwan, S. K. Song, Y. Huang, W. Z. Ray, J. A. Rogers, *Nat. Biomed. Eng.* **2019**, 3, 37.
- [10] Q. S. Yang, S. Lee, Y. G. Xue, Y. Yan, T. L. Liu, S. K. Kang, Y. J. Lee, S. H. Lee, M. H. Seo, D. Lu, J. Koo, M. R. MacEwan, R. S. T. Yin, W. Z. Ray, Y. G. Huang, J. A. Rogers, *Adv. Funct. Mater.* **2020**, 30, 1910718.
- [11] L. Yin, H. Cheng, S. Mao, R. Haasch, Y. Liu, X. Xie, S.-W. Hwang, H. Jain, S.-K. Kang, Y. Su, R. Li, Y. Huang, J. A. Rogers, *Adv. Funct. Mater.* **2014**, 24, 645.
- [12] S.-K. Kang, S.-W. Hwang, H. Cheng, S. Yu, B. H. Kim, J.-H. Kim, Y. Huang, J. A. Rogers, *Adv. Funct. Mater.* **2014**, 24, 4427.
- [13] Y. K. Lee, K. J. Yu, E. Song, A. Barati Farimani, F. Vitale, Z. Xie, Y. Yoon, Y. Kim, A. Richardson, H. Luan, Y. Wu, X. Xie, T. H. Lucas, K. Crawford, Y. Mei, X. Feng, Y. Huang, B. Litt, N. R. Aluru, L. Yin, J. A. Rogers, *ACS Nano* **2017**, 11, 12562.
- [14] L. S. Nair, C. T. Laurencin, *Prog. Polym. Sci.* **2007**, 32, 762.
- [15] S. M. Won, J. Koo, K. E. Crawford, A. D. Mickle, Y. Xue, S. Min, L. A. McIlvried, Y. Yan, S. B. Kim, S. M. Lee, B. H. Kim, H. Jang, M. R. MacEwan, Y. Huang, R. W. Gereau, J. A. Rogers, *Adv. Funct. Mater.* **2018**, 28, 1801819.
- [16] a) M. S. Kim, J. S. Jeong, H. S. Ryu, S. H. Choi, S. J. Chung, *J. Neurol. Sci.* **2017**, 383, 135; b) M. Rosa, E. Scelzo, M. Locatelli, G. Carrabba, V. Levi, M. Arlotti, S. Barbieri, P. Rampini, A. Priori, *World Neurosurg.* **2017**, 97, 64.
- [17] C. M. Boutry, L. Beker, Y. Kaizawa, C. Vassos, H. Tran, A. C. Hinckley, R. Pfattner, S. Niu, J. Li, J. Claverie, Z. Wang, J. Chang, P. M. Fox, Z. Bao, *Nat. Biomed. Eng.* **2019**, 3, 47.
- [18] M. Luo, A. W. Martinez, C. Song, F. Herrault, M. G. Allen, *J. Microelectromech. Syst.* **2014**, 23, 4.
- [19] L. Yin, X. Huang, H. Xu, Y. Zhang, J. Lam, J. Cheng, J. A. Rogers, *Adv. Mater.* **2014**, 26, 3879.
- [20] Q. A. Huang, L. Dong, L. F. Wang, *J. Microelectromech. Syst.* **2016**, 25, 822.
- [21] G. L. Bloomfield, P. C. Ridings, C. R. Blocher, A. Marmarou, H. J. Sugerman, *Crit. Care Med.* **1997**, 25, 496.
- [22] X. Meng, K. D. Browne, S.-M. Huang, C. Mietus, D. K. Cullen, M.-R. Tofighi, A. Rosen, *IEEE Tran. Microwave Theory Techn.* **2013**, 61, 316.
- [23] G. Voskerician, M. S. Shive, R. S. Shawgo, H. von Recum, J. M. Anderson, M. J. Cima, R. Langer, *Biomaterials* **2003**, 24, 1959.
- [24] a) J. Koo, M. R. MacEwan, S.-K. Kang, S. M. Won, M. Stephen, P. Gamble, Z. Xie, Y. Yan, Y.-Y. Chen, J. Shin, N. Birenbaum, S. Chung, S. B. Kim, J. Khalifeh, D. V. Harburg, K. Bean, M. Paskett, J. Kim, Z. S. Zohny, S. M. Lee, R. Zhang, K. Luo, B. Ji, A. Banks, H. M. Lee, Y. Huang, W. Z. Ray, J. A. Rogers, *Nat. Med.* **2018**, 24, 1830; b) W. Bai, J. Shin, R. Fu, I. Kandela, D. Lu, X. Ni, Y. Park, Z. Liu, T. Hang, D. Wu, Y. Liu, C. R. Haney, I. Stepien, Q. Yang, J. Zhao, K. R. Nandoliya, H. Zhang, X. Sheng, L. Yin, K. MacRenaris, A. Brikha, F. Aird, M. Pezhouh, J. Hornick, W. Zhou, J. A. Rogers, *Nat. Biomed. Eng.* **2019**, 3, 644; c) C. Kampmann, R. Brzezinska, M. Abidini, A. Wenzel, C.-F. Wippermann, P. Habermehl, M. Knuf, R. Schumacher, *Pediatr. Radiol.* **2002**, 32, 839; d) J. M. Maloney, S. A. Lipka, S. P. Baldwin, *MRS Proc.* **2005**, 872, J14.3.